Atomic data of Cu i for the investigation of element abundance

Article *in* The Astrophysical Journal Supplement Series · April 2014

Impact Factor: 11.22 · DOI: 10.1088/0067-0049/211/2/30

The Astrophysical Journal Supplement Series, 211:30 (11pp), 2014 April doi:10.1088/0067-0049/211/2/30

ATOMIC DATA OF Cu I FOR THE INVESTIGATION OF ELEMENT ABUNDANCE

Y. P. Liu[1], C. Gao[1], J. L. Zeng[1], J. M. Yuan[1], and J. R. Shi[2]
[1] Department of Physics, College of Science, National University of Defense Technology, Changsha 410073, China; jiaolongzeng@hotmail.com
[2] National Astronomical Observatories, Chinese Academy of Sciences, Beijing 100012, China
Received 2013 December 31; accepted 2014 February 11; published 2014 April 2

ABSTRACT

A complete set of atomic data of Cu I, including the energy levels, oscillator strengths, and photoionization cross sections, is theoretically studied to investigate element abundance including nonlocal thermodynamic equilibrium (NLTE) effects. The calculations are carried out by using the *R*-matrix method in the *LS*-coupling scheme. Twenty terms of Cu II are utilized as target states, and extensive configuration interactions are included to properly delineate the quantum states of Cu II and Cu I. One hundred thirteen bound states and 1699 oscillator strengths for E1 transitions between these states are obtained. Photoionization cross sections for all bound states are calculated in a photon energy range covering 1.28 Ry from the threshold of the respective state. Resonances shown in the photoionization cross sections are identified, and some strong resonances are expected to play an important role in NLTE modeling. The atomic data in this work represent the first complete data set for copper abundance studies. Our results are compared with the experimental and other theoretical data wherever available.

Key words: atomic data – line: formation – stars: abundances

Online-only material: color figures, supplemental data

1. INTRODUCTION

The abundance of copper plays an important role in the investigations of the chemical evolution of various stars, such as giant stars (McWilliam & Smecker-Hane 2005) and solar-type stars (Brewer & Carney 2006). It was found that copper had a behavior quite different from other Fe-peak elements both in our Galaxy (Simmerer et al. 2003) and in extragalactic systems (Johnson et al. 2006). Moreover, the [Cu/Fe] ratios show a decreasing trend in the low-metallicity region in Galactic stars except those of the globular cluster ω Centauri (Bisterzo et al. 2004; Romano & Matteucci 2007), whereas they show no discernible trend and are significantly subsolar in the Large Magellanic Cloud (Johnson et al. 2006; Colucci et al. 2012), the Sagittarius dwarf spheroidal galaxy (McWilliam & Smecker-Hane 2005), and ω Centauri (Cunha et al. 2002). Such peculiarities have led to a complicated nucleosynthesis model of copper (Bisterzo et al. 2004; Allen & Porto de Mello 2011) and make the abundance of copper a possible clue for the origins of globular clusters (McWilliam & Smecker-Hane 2005) and the evolution of galaxies (Colucci et al. 2012). Accurate determination of the abundance of copper helps clarify these problems.

Asplund (2005) pointed out that it was important to include the effects of nonlocal thermodynamic equilibrium (NLTE) when determining element abundances. Investigations confirmed that the abundances of Na, Mg, Al, Si, K, Ca, Mn, and Co were considerably affected by the NLTE effects (Gehren et al. 2006; Shi et al. 2008; Mashonkina et al. 2008; Cunha et al. 2010; Bergemann et al. 2010). Copper is an element whose interesting evolution with metallicity is not fully understood. In the investigation of Cu I resonance lines in turnoff stars of NGC 6752 and NGC 6397, Bonifacio et al. (2010) pointed out that departures from NLTE should be taken into account to properly describe these lines. As a result, NLTE effects should be included in the accurate determination of Cu abundance in both dwarfs and giants. However, to the best of our knowledge, there are no such abundance studies of copper including NLTE effects up to now. Building an adequate NLTE model requires a complete set of accurate atomic data involving a large number of quantum states of a complete set of bound energy levels. Moreover, higher processes such as direct double photoionization and Auger decay (Zeng et al. 2013a, 2013b) may also play a role in the NLTE model (Xiang et al. 2012). Up to now, to the best of our knowledge, there is no such complete set of atomic data to utilize for the copper abundance investigation. The main reason may be due to the complex electronic structure of copper. Shi et al. (2014) carried out the first study on the NLTE effects on the solar abundance of copper by using the preliminary results of the present work.

The complexity of the electronic structure of copper can be seen from Figure 1, which shows the energy levels of Cu I together with energy levels for some low-lying terms of Cu II utilized as target states in the present work. The data in Figure 1 were derived from spectrum observations and experiments (Sugar & Musgrove 1990). For both Cu I and Cu II, the energies of $3d$ and $4s$ orbitals are very close, and their competition results in complex energy levels. For Cu I, in the *LS*-coupling scheme, there are 10 bound states belonging to the $3d$ excited configurations $[1s^2 2s^2 2p^6 3s^2 3p^6]3d^9 4s^2$ and $3d^9 4s4p$. This makes Cu I an opening $3d$ atomic system, which is difficult to deal with theoretically because of the strong electron correlations, especially in the calculations of transition probabilities for the perturbed Rydberg states $3d^{10}np^2\,P^o$ (Carlsson 1988; Biémont et al. 1996). The lowest excited state $3d^9 4s^2\,{}^2D$ is a metastable state, and its energy level is just about 0.1 Ry relative to the ground state. Such a long-lived state with very low energy is very important in the NLTE model, yet the available atomic data are quite scarce. For Cu II, the terms of the two-electron excitation configuration $3d^8 4s^2$ are bound ones, and their energies span a wide range from 0.6473 to 1.2862 Ry. As is well known, theoretical treatment of such two hole states is a challenge for atomic theory.

Experimental measurements of the transition probabilities and oscillator strengths of Cu I were mainly focused on the excitations from the three lowest states in Figure 1 to final states with principal quantum numbers lower than 6 (Fu et al. 1995).

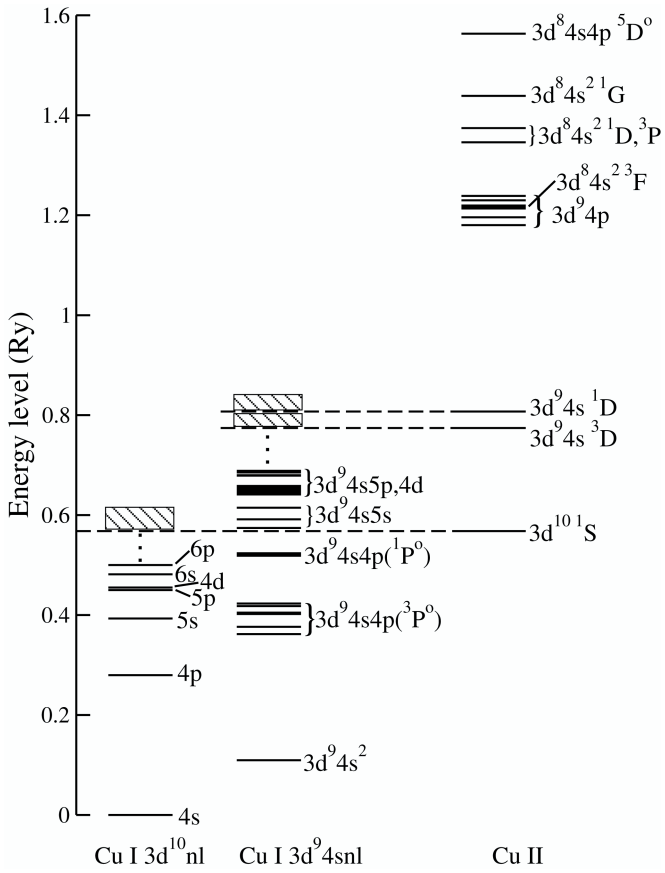

Figure 1. Level structure for Cu I and Cu II (relative to the ground state $3d^{10}4s\ ^2S$ of Cu I). Experimental data are taken from Sugar & Musgrove (1990).

Froese Fischer (1977) calculated the oscillator strength of the resonance transition $3d^{10}4s\ ^2S$–$3d^{10}4p\ ^2P^o$ in both length and velocity forms by using the multiconfiguration Hartree–Fock (MCHF) method, and Migdałek (2002) and Owono Owono et al. (2005) studied the core polarization effects on this transition with a model potential approach and a quantum-defect approximation, respectively. Lindgård et al. (1980), Carlsson (1988), and Zheng et al. (2000) calculated the relevant data for the transition arrays of the series $3d^{10}nl$ with higher n for s, p, and d states. Recently, Civiš et al. (2011b) investigated higher l transitions involving f and g states. For transitions of states belonging to $3d^94s^2$ and $3d^94s4p$, few theoretical investigations have been reported in the literature.

Photoionization cross sections of Cu I are quite lacking both experimentally and theoretically compared to the oscillator strengths of bound–bound transitions. Verweyen et al. (1998) calculated the photoionization of Cu I in the region of the $3p$ inner-shell threshold within the R-matrix theory in order to explain the experiments of the excitation from the $3p$ inner shell (Bruhn et al. 1979). The photoabsorption spectrum below the threshold $3d^94s\ ^1D$ was measured using different experimental methods (Tondello 1973; Müller et al. 1986; Baig et al. 1997), and the autoionization states of the series $3d^94snp$ ($n \geqslant 5$) attracted great attention. Liu et al. (1994) calculated photoionization cross sections of $4s$, $3d$, and $3p$ subshells in energy regions beyond 100 eV with many-body perturbation theory (MBPT). However, all these investigations are limited to the ground state $3d^{10}4s\ ^2S$ of Cu I. To the best of our knowledge, no investigations were reported for the photoionization cross sections of the excited states of Cu I.

In this paper, we aim to present a complete set of atomic data including the energy levels, oscillator strengths, and photoionization cross sections of Cu I for NLTE modeling in the copper abundance investigation of astrophysical objects. These basic atomic data are also important in calculations of radiative opacity of hot, dense plasmas (Zeng & Yuan 2006, 2007; Zeng 2008; Zeng et al. 2010). Our calculations are carried out in the LS-coupling scheme by using the R-matrix program,[3] which is a modified version of the Belfast atomic R-matrix program RMATRX1 (Berrington et al. 1995). Fourteen terms belonging to the configurations of $3d^{10}$, $3d^94s$, $3d^94p$, and $3d^84s^2$ and the lowest six terms belonging to $3d^84s4p$ of Cu II are utilized as target states. Extensive configuration interaction (CI) effects are taken into account to ensure that atomic data that are as accurate as possible can be obtained.

2. THEORETICAL METHODS

The R-matrix method is powerful for analyzing electron–atom collision and photoionization and has been widely employed to obtain the relevant atomic data (Bautista 2000; Liang & Badnell 2010; Liu et al. 2011). A detailed description of the R-matrix theory can be found in Berrington et al. (1995); below we only give an outline of this method. The R-matrix method starts by partitioning space into two regions by a definite sphere of radius centered on the target nucleus, whose value is chosen such that all bound orbitals included in the calculations are suitably small at the boundary. In the internal region, energy-independent basis states of the entire $(N + 1)$-electron system are expanded in the form

$$\psi_k(X_1 \ldots X_{N+1}) = \hat{A} \sum_{ij} c_{ijk} \overline{\Phi}_i(X_1 \ldots X_N \hat{r}_{N+1} \sigma_{N+1}) \times r_{N+1}^{-1} u_{ij}(r_{N+1}) + \sum_j d_{jk} \phi_j(X_1 \ldots X_{N+1}), \quad (1)$$

where $\hat{A}$ is the antisymmetrization operator, which accounts for electron exchange between the N electrons of the target and the free electron, and i is the channel symbol. X_m stands for the spatial ($\boldsymbol{r}_m$) and the spin (σ_m) coordinates of the mth electron. The continuum orbitals $u_{ij}(r)$, which represent the motion of the scattered electron, are the only terms that are nonzero on the surface of the internal region. In the external region, the exchange effects between the target electrons and the scattered electron are ignored.

To properly consider the electron correlation, target states Φ_i are expressed in a CI expansion

$$\Phi_i(X_1 \ldots X_N) = \sum_k b_{ik} \varphi_k(X_1 \ldots X_N), \quad (2)$$

where φ_k are the configuration state functions (CSF) constructed from the one-electron orbitals of bound states. The radial functions $P_{nl}(r)$ are represented as linear combinations of Slater-type orbitals with the required parameters being determined by a variational optimization on the energies of specific LS-coupled states.

The present calculation employs 11 orbitals of Cu II. Orbitals $1s$, $2s$, $2p$, $3s$, $3p$, $3d$, and $4s$ are chosen to be the Hartree–Fock (HF) functions given by Clementi & Roetti (1974) for Cu II excited state $3d^84s^2\ ^3F$. We also testified the HF functions of

[3] http://amdpp.phys.strath.ac.uk/tamoc/code.html

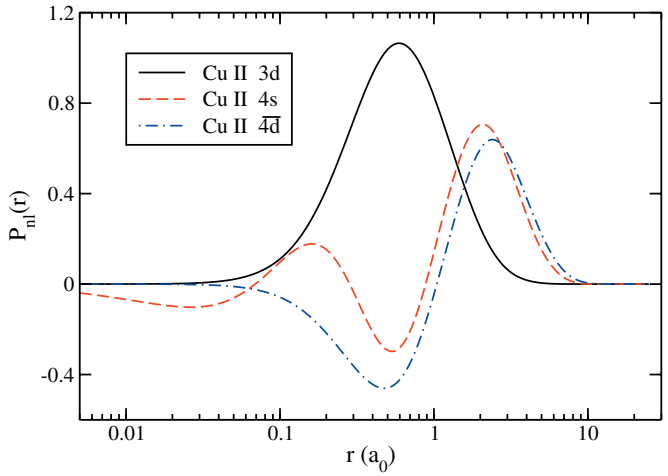

Figure 2. Radial wave functions for the orbitals of $3d$, $4s$, and $\overline{4d}$ of Cu II.
(A color version of this figure is available in the online journal.)

the ground state $3d^{10}\ ^1S$, yet we found that the relative energies of the target states belonging to $3d^8 4s^2$ were worse compared with the experimental results. Hence, we start our calculations from the HF functions of $3d^8 4s^2\ ^3F$. The $4p$ and $5s$ orbitals are spectroscopic orbitals obtained by using the program CIV3 (Hibbert 1975), while the two correlation orbitals $\overline{4d}$ and $\overline{5p}$ are obtained by optimizing $3d^{10}\ ^1S$ and $3d^9 4p\ ^1F^o$, respectively. In Figure 2, we show the radial wave functions of $3d$, $4s$, and $\overline{4d}$. It can be seen that there is a strong overlap between the orbitals of $3d$ and $4s$, which is an important source of the complex atomic structure of copper. The correlation orbital $\overline{4d}$ is contractive to the region of $3d$ and $4s$, which is expected to play an important role in dealing with the electron correlations. For the construction of the continuum states, the number of the continuum basis functions $u_{ij}(r)$ is set to 40 for each angular momentum from 0 to 8. The R-matrix radius is chosen to be 28.0 au to ensure that the wave functions of bound states are completely wrapped within the R-matrix sphere.

In this work, CIs among $3d^{10}$, $3d^9 nl$, $3d^8 nln'l'$, $3d^7 4snln'l'$ (nl, $n'l'$ can be $4s$, $4p$, $\overline{4d}$, $5s$, $\overline{5p}$), and $3d^7 4d^3$ are included to describe the target states. Coefficients b_{ik} in Equation (2) are determined by diagonalizing the Hamiltonian of Cu II for each symmetry. In Table 1, as illustrative examples, we give the dominant mix coefficients with absolute values greater than 0.1 for the six lowest target states. It can be seen that these terms have a strong correlations with those of the $\overline{4d}$ orbital, especially for the ground state $3d^{10}\ ^1S$. In Table 2 we compare the calculated energy levels of the 20 target states with the experimental results (Kramida et al. 2012). Generally good agreement is found between the theory and experiment, with the largest relative difference being 6.13%.

Table 1
Mix Coefficients b_{ik} in Equation (2) for the Lowest Six Target States

Symmetry	CSF	b_{ik}
^1S	$3d^{10}$	0.8158
	$3d^9\overline{4d}$	0.5643
^3D	$3d^9 4s$	0.9397
	$3d^8 4s[^4F]\overline{4d}$	−0.2208
	$3d^8 4s[^2G]\overline{4d}$	−0.1145
	$3d^8 4s[^4P]\overline{4d}$	−0.1098
^1D	$3d^9 4s$	0.9386
	$3d^8 4s[^2F]\overline{4d}$	−0.2564
	$3d^8 4s[^2P]\overline{4d}$	−0.1306
$^3P^o$	$3d^9 4p$	0.9381
	$3d^8(^3F)4p[^4D^o]\overline{4d}$	−0.1668
	$3d^9\overline{5p}$	0.1382
	$3d^8(^3F)4p[^4F^o]\overline{4d}$	−0.1281
	$3d^8(^1G)4p[^2F^o]\overline{4d}$	−0.1157
$^3F^o$	$3d^9 4p$	0.9410
	$3d^8(^3F)4p[^4G^o]\overline{4d}$	−0.1846
	$3d^9\overline{5p}$	0.1192
^3F	$3d^8 4s^2$	0.9715
	$3d^8(^3F)4p^2(^1S)$	0.1758

Note. Only those with absolute values larger than 0.1 are listed.

Table 2
Energies (in Ry) for the Target States of Cu II (Relative to the Ground State)

Target State	This Work	NIST	Diff.(%)
$3d^{10}\ ^1S$	0.0	0.0	0.0
$3d^9 4s\ ^3D$	0.2039	0.2064	1.20
$3d^9 4s\ ^1D$	0.2356	0.2393	1.58
$3d^9 4p\ ^3P^o$	0.6427	0.6123	4.96
$3d^8 4s^2\ ^3F$	0.6578	0.6473	1.63
$3d^9 4p\ ^3F^o$	0.6624	0.6279	5.49
$3d^9 4p\ ^1F^o$	0.6697	0.6456	3.74
$3d^9 4p\ ^1D^o$	0.6864	0.6515	5.36
$3d^9 4p\ ^3D^o$	0.6875	0.6619	3.87
$3d^9 4p\ ^1P^o$	0.7103	0.6707	5.91
$3d^8 4s^2\ ^1D$	0.8258	0.7781	6.13
$3d^8 4s^2\ ^3P$	0.8474	0.8065	5.06
$3d^8 4s^2\ ^1G$	0.9137	0.8709	4.92
$3d^8(^3F)4s4p(^3P^o)\ ^5D^o$	0.9687	0.9954	2.68
$3d^8(^3F)4s4p(^3P^o)\ ^5G^o$	0.9849	1.0300	4.38
$3d^8(^3F)4s4p(^3P^o)\ ^5F^o$	1.0046	1.0339	2.83
$3d^8(^3F)4s4p(^3P^o)\ ^3G^o$	1.0258	1.0550	2.77
$3d^8(^3F)4s4p(^3P^o)\ ^3D^o$	1.0434	1.0674	2.24
$3d^8(^3F)4s4p(^3P^o)\ ^3F^o$	1.0491	1.0767	2.56
$3d^8 4s^2\ ^1S$	1.2862		

Note. Experimental data (Kramida et al. 2012) are given for comparison.

3. RESULTS AND DISCUSSION

Using the method described above, we calculated the energy levels of the bound states, bound–bound oscillator strengths, and photoionization cross sections of Cu I.

3.1. Bound States of Cu I

In total, 113 bound states of Cu I are obtained, and 10 of them belong to $3d$ excited configurations of $3d^9 4s^2$ and $3d^9 4s4p$. In Table 3, the theoretical energy levels in the present work are compared with the experimental results (Kramida et al. 2012; Civiš et al. 2011a) wherever available. Very good agreement can be found between the theory and experiment for the series of $3d^{10}nl$, with the relative difference being about 1% for most states. The calculated ionization potential of the ground state $3d^{10}4s\ ^2S$ (0.5699 Ry) is very close to the experimental value (0.5679 Ry). For states belonging to the series $3d^9 4snl$, a slightly larger discrepancy was found. The energy level of $3d^9 4s^2\ ^2D$ is a little higher than that in Kramida et al. (2012), while the states of $3d^9 4s4p(^3P^o)$ are slightly lower than those in Kramida et al.

Table 3
Comparison between the Calculated and Experimental (Kramida et al. 2012; Civiš et al. 2011a) Energy Levels (in Ry) of Cu I

State	n_e	Theory	Experiment
$3d^{10}4s\ ^2S$	1.3246	0.0	0.0
$3d^94s^2\ ^2D$	1.4902	0.1196	0.1095
$3d^{10}4p\ ^2P^o$	1.8311	0.2717	0.2798
$3d^94s4p(^3P^o)\ ^4P^o$	1.5237	0.3431	0.3618
$3d^94s4p(^3P^o)\ ^4F^o$	1.5573	0.3615	0.3765
$3d^94s4p(^3P^o)\ ^2F^o$	2.3344	0.3864	0.4049
$3d^94s4p(^3P^o)\ ^4D^o$	1.6130	0.3895	0.4021
$3d^{10}5s\ ^2S$	2.4162	0.3986	0.3931
$3d^94s4p(^3P^o)\ ^2P^o$	2.4667	0.4056	0.4179
$3d^94s4p(^3P^o)\ ^2D^o$	1.6491	0.4061	0.4231
$3d^{10}5p\ ^2P^o$	2.9120	0.4520	0.4500
$3d^{10}4d\ ^2D$	3.0076	0.4594	0.4551
$3d^{10}6s\ ^2S$	3.4299	0.4849	0.4816
$3d^{10}6p\ ^2P^o$	3.8610	0.5028	0.5000
$3d^{10}4f\ ^2F^o$	3.9924	0.5072	0.5051
$3d^{10}5d\ ^2D$	4.0129	0.5078	0.5048
$3d^{10}7s\ ^2S$	4.4349	0.5191	0.5164
$3d^94s4p(^1P^o)\ ^2F^o$	4.5450	0.5215	0.5187
$3d^94s4p(^1P^o)\ ^2P^o$	4.5821	0.5223	0.5196
$3d^94s4p(^1P^o)\ ^2D^o$	2.0123	0.5269	0.5237
$3d^{10}5f\ ^2F^o$	4.9932	0.5298	0.5277
$3d^{10}5g\ ^2G$	4.9984	0.5299	0.5279*
$3d^{10}6d\ ^2D$	5.0148	0.5301	0.5276
$3d^{10}7p\ ^2P^o$	5.1513	0.5322	0.5265
$3d^{10}8s\ ^2S$	5.4371	0.5361	0.5337
$3d^{10}6f\ ^2F^o$	5.9919	0.5421	0.5400*
$3d^{10}6g\ ^2G$	5.9981	0.5421	0.5401*
$3d^{10}6h\ ^2H^o$	5.9997	0.5421	0.5401*
$3d^{10}7d\ ^2D$	6.0154	0.5423	0.5399
$3d^{10}8p\ ^2P^o$	6.0432	0.5425	0.5403
$3d^{10}9s\ ^2S$	6.4383	0.5458	0.5436
$3d^{10}7f\ ^2F^o$	6.9914	0.5494	0.5474*
$3d^{10}7g\ ^2G$	6.9980	0.5495	0.5475*
$3d^{10}7h\ ^2H^o$	6.9995	0.5495	
$3d^{10}8d\ ^2D$	7.0155	0.5496	0.5474
$3d^{10}9p\ ^2P^o$	7.0171	0.5496	0.5474
$3d^{10}8f\ ^2F^o$	7.9911	0.5542	0.5522
$3d^{10}8g\ ^2G$	7.9979	0.5543	
$3d^{10}8h\ ^2H^o$	7.9994	0.5543	
$3d^{10}10p\ ^2P^o$	8.0066	0.5543	0.5522
$3d^{10}9d\ ^2D$	8.0156	0.5543	0.5522
$3d^{10}9f\ ^2F^o$	8.9909	0.5575	
$3d^{10}9g\ ^2G$	8.9978	0.5576	
$3d^{10}9h\ ^2H^o$	8.9993	0.5576	
$3d^{10}11p\ ^2P^o$	9.0011	0.5576	0.5555
$3d^{10}12p\ ^2P^o$	9.9978	0.5599	0.5578
$3d^{10}17p\ ^2P^o$	14.9914	0.5655	0.5634
$3d^{10}22p\ ^2P^o$	19.9896	0.5674	0.5654
Cu II(^1S)Limit		0.5699	0.5679

Note. The effective principal quantum number n_e obtained in the present calculation are also given.

* The experimental data with $*$ are taken from Civiš et al. (2011a), and others are from Kramida et al. (2012).

(2012). Such good agreement is an indication of the accuracy of relevant wave function.

The second column of Table 3 gives the effective principle quantum number n_e of each bound state obtained in the present work, from which the quantum defect δ ($\delta = n - n_e$) can be determined. In Figure 3, we present the quantum defects of the Rydberg series $3d^{10}nl$, where $n \leqslant 22$ for $l = 0, 1$ and $n \leqslant 20$ for $l = 2$–5. The quantum defect of the largest n for each

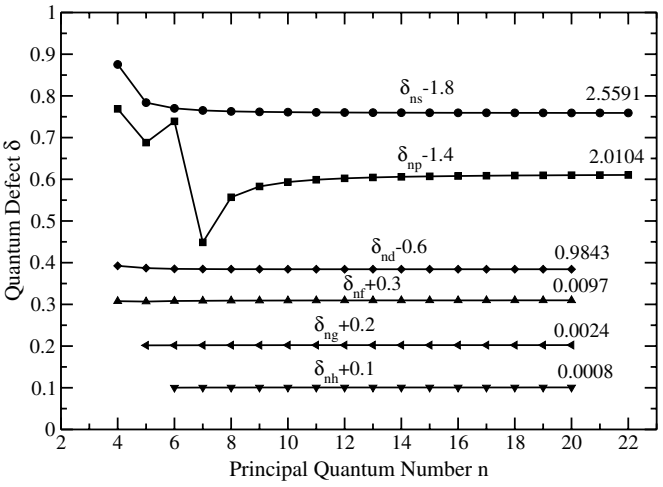

Figure 3. Quantum defect of Rydberg series $3d^{10}nl$ ($l = 0$–5). For better viewing, data for each series have been shifted by a constant shown in the figure. The value indicated at the end of each curve is the quantum defect of the largest n for the respective series.

Rydberg series is given at the end of respective curve. For better viewing, the quantum defect of each Rydberg series is shifted by a proper value shown in the figure. Inspecting Figure 3, one can see that there are no or few perturbing effects of other states that affect the Rydberg series $3d^{10}nd$, $3d^{10}nf$, $3d^{10}ng$, and $3d^{10}nh$, and thus, their quantum defects show smooth functions of n with little variation. Actually, the interloper of $3d^94s^2\ ^2D$ influences the $3d^{10}nd$ series, and so do $3d^94s4p(^3P^o)\ ^2F^o$ and $3d^94s4p(^1P^o)\ ^2F^o$ for $3d^{10}nf$, but they do not show evident effects. Moreover, the behaviors of the $3d^{10}nf$, $3d^{10}ng$, and $3d^{10}nh$ series are hydrogenic, with the maximal quantum defect being less than 0.01. However, for the Rydberg series of $3d^{10}np$, the case is completely different. The quantum defect of this series shows an oscillatory characteristic for $n \leqslant 10$, which means that there are other strong interlopers affecting this series. Indeed, this series is strongly perturbed by $3d^94s4p(^3P^o)\ ^2P^o$ and $3d^94s4p(^1P^o)\ ^2P^o$. As our calculated energy levels agree well with the experimental results, which can be seen from Table 3, the quantum defects shown in Figure 3 are accurate and represent the true physical situation for Cu I. Such a fact implies that there are strong electron correlations between the configurations of $3d^{10}np$ and $3d^94s4p$, and therefore, the single configuration approximation for the $3d^{10}np$ series is completely invalid. This is also the physical origin of the large discrepancy between calculations with different methods for the oscillator strengths of the transition array $3d^{10}ns$–$3d^{10}np$, which will be discussed in the next section.

3.2. Oscillator Strengths

Oscillator strengths are obtained for 1699 dipole allowed transitions between the 113 bound states of Cu I. The weighted oscillator strengths (gf values) are calculated in both the length and velocity forms, except that only the length form is given for transitions whose energy interval is too small. To evaluate the quality of the calculated oscillator strengths, the velocity form versus the length form of the absolute gf values greater than 0.001 are displayed in Figure 4. Since the data cover five orders of magnitude, we adopt the logarithm coordinates. It can be seen that generally good agreement is found between the length and velocity forms of the oscillator strengths, especially for the larger values.

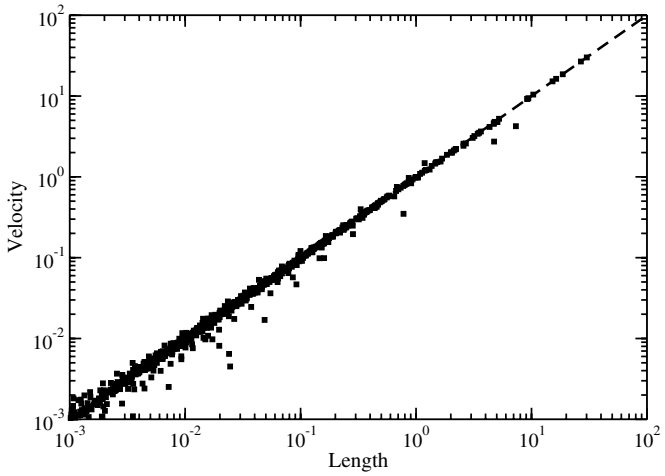

Figure 4. Velocity vs. length forms for the gf values of Cu I.

In Table 4, the theoretical weighted oscillator strengths in the length form are compared with the available experimental and other theoretical results. Most experimental results were obtained for transitions between the fine-structure levels; for comparison we convert the results from fine-structure levels to LS-coupled terms according to the statistical method by summing all possible levels belonging to the final term and averaging all possible levels belonging to the initial term. The data of Kramida et al. (2012) were mainly taken from the compilation of Wiese & Martin (1980), and those offered by Kurucz & Bell (1995) were taken from Bielski (1975), Corliss (1970), and the calculation of Biémont (1973). The results of Biémont (1973) were very close to those of Lindgård et al. (1980) because they used the same theoretical method. Therefore, the data presented by Kramida et al. (2012) and Kurucz & Bell (1995) are not given in Table 4.

Table 4 shows that our results are in generally good agreement with the experimental data for the strong transitions. Our gf value of the resonance transition $3d^{10}4s\ ^2S$–$3d^{10}4p\ ^2P^o$ (1.3330) agrees well with all experimental values (Hannaford & Lowe 1983; Wiese & Martin 1980; Bielski 1975; Siefart et al. 1974; Corliss 1970), and the theoretical results (Civiš et al. 2011b; Owono Owono et al. 2005; Migdałek 2002; Curtis & Theodosiou 1989; Carlsson 1988; Lindgård et al. 1980; Froese Fischer 1977; Chou & Johnson 1997) also converge with the experimental values. A similar conclusion can be drawn for $3d^{10}5s$, $6s\ ^2S$–$3d^{10}4p\ ^2P^o$ and $3d^{10}4p\ ^2P^o$–$3d^{10}4d\ ^2D$, yet our gf value for $3d^{10}4s\ ^2S$–$3d^94s4p(^3P^o)\ ^2P^o$ is a little larger than the experimental results and the only theoretical value (Carlsson 1988). For the transition of $3d^94s^2\ ^2D$–$3d^{10}4p\ ^2P^o$, which is also important in the investigation of copper abundance (Bonifacio et al. 2010), our gf value of 0.0501 is in good agreement with the experimental results. Transitions from $3d^94s^2\ ^2D$ to $3d^94s4p(^3P^o)\ ^2F^o$, $^2P^o$, and $^2D^o$ show a larger discrepancy between the theory and experiments. However, there is also an evident discrepancy between different experimental values, which implies the difficulty in accurately measuring the oscillator strengths of these transitions. For all the transitions of the metastable state $3d^94s^2\ ^2D$, to our knowledge, there is no other theoretical investigation reported in the literature. However, the atomic data involving this term are vital in studies of copper abundance.

Below we discuss the comparison between our weighted oscillator strengths and other theoretical results. For the transition arrays of $3d^{10}np\ ^2P^o$–$3d^{10}md\ ^2D$, $3d^{10}nd\ ^2D$–$3d^{10}mf\ ^2F^o$, and $3d^{10}nf\ ^2F^o$–$3d^{10}mg\ ^2G$, there is good agreement between our gf values and other calculations (Lindgård et al. 1980; Civiš et al. 2011b). However, for the transition series of $3d^{10}ns\ ^2S$–$3d^{10}mp\ ^2P^o$, the case is different. For the strong transitions with gf values larger than 0.3, good agreements are found between all theoretical results. However, for the weak transitions, large discrepancies are found between different theoretical methods. Take $3d^{10}4s\ ^2S$–$3d^{10}mp\ ^2P^o$ as an example. The only strong transition is $3d^{10}4s\ ^2S$–$3d^{10}4p\ ^2P^o$, and different theoretical methods obtained basically consistent gf values, but large differences are found for the transitions of $3d^{10}4s\ ^2S$–$3d^{10}mp\ ^2P^o$ ($m = 5$–9). We take $3d^{10}4s\ ^2S$–$3d^{10}5p\ ^2P^o$ to illustrate the case. By using the MCHF method with the first-order relativistic effects, Carlsson (1988) obtained a gf value of 0.0994, which was much larger than the result of 0.0526 obtained by Lindgård et al. (1980) and 0.0224 obtained by Zheng et al. (2000). Lindgård et al. (1980) employed a semiempirical method to obtain the oscillator strengths by using the experimental energy levels and ionization potential as inputs. Zheng et al. (2000) performed their calculation with a weakest bound electron potential model. As indicated above, the Rydberg series $3d^{10}np\ ^2P^o$ are strongly perturbed by $3d^94snp$ and $3d^84s^2np$ (in particular $3d^94s4p$), and therefore, complete calculations including these perturbing configurations are vital to obtain accurate energy levels and oscillator strengths. In his theoretical work, Carlsson (1988) took the CI effects of $3d^94s4p$, $3d^94s4f$, and $3d^84s^24p$ into account, which is the best consideration of CI effects among other theoretical works. In our R-matrix calculation, we have included a more complete treatment of CI by including configurations of $3d^94s4p$, $3d^94p5s$, $3d^94p\overline{4d}$, $3d^94s\overline{5p}$, and $3d^84s^2\overline{5p}$ and the continuum states $3d^94skp, kf$, $3d^94pks, kd$, and $3d^84s^2kp, kf$. Hence, we believe that the results of such a calculation should be more accurate.

3.3. Photoionization Cross Sections

In stellar atmospheres, photoionization of neutral species is crucial in an abundance determination that accounts for the NLTE effects (Asplund 2005). Photoionization cross sections are more important for the ground and several lowest excited states. In the following, we present in detail the photoionization cross sections of the ground state ($3d^{10}4s\ ^2S$) and three lowest excited states ($3d^94s^2\ ^2D$, $3d^{10}4p\ ^2P^o$, and $3d^94s4p(^3P^o)\ ^4P^o$) of Cu I. Photoionization cross sections of $3d^{10}ns\ ^2S$ ($n = 5$–8) are also presented to show the general trend of a Rydberg series. For all 113 bound states, partial wave and the total photoionization cross sections are calculated in a photon energy range covering 1.28 Ry from the respective threshold. Such an energy range is sufficient to investigate the abundance of copper.

Figure 5 shows the photoionization cross section of the ground state $3d^{10}4s\ ^2S$. The solid and dashed lines represent the length and velocity forms, respectively. The dotted line is the total cross section of the $3d$ and $4s$ subshells calculated with the MBPT method (Liu et al. 1994). Below the third threshold, $3d^94s\ ^1D$ (0.8055 Ry), there are many strong autoionization resonances, which are displayed on an expanded scale in the inset and identified as the resonant series $3d^94s(^{3,1}D)np\ ^2P^o$ and $3d^94s(^{3,1}D)nf\ ^2P^o$. The resonances of $3d^94s(^3D)6p\ ^2P^o$ and $3d^94s(^3D)4f\ ^2P^o$ are indistinguishable from each other because of their overlap, and so are $3d^94s(^3D)7p\ ^2P^o$ and $3d^94s(^3D)4f\ ^2P^o$. Above the third threshold, $3d^94s\ ^1D$, there are weak resonances of the two-electron excitation states, such

Table 4
The gf Values Compared with the Experimental and Other Theoretical Results

Transition	This Work	Experiments[a]	Other Theory
$3d^{10}4s\ ^2S$—$3d^{10}4p\ ^2P^o$	1.3330	1.308(36)[a], 1.32(13)[b], 1.317[c], 1.310[d], 1.338[e]	1.3449[h],1.3362[i], 1.2920[j], 1.3386[k], 1.3934[l], 1.5856[m], 1.2472[n], 1.3766[o]
$3d^9 4s4p(^3P^o)\ ^2P^o$	0.5641	0.403(42)[b], 0.436[c], 0.492[d], 0.328[e], 0.402(58)[f]	0.4276[l]
$3d^{10}5p\ ^2P^o$	0.0240		0.0994[l], 0.0526[m], 0.0224[p]
$3d^{10}6p\ ^2P^o$	0.0156		0.0235[l], 0.0020[m], 0.0012[p]
$3d^9 4s4p(^1P^o)\ ^2P^o$	0.1293		0.0745[l]
$3d^{10}7p\ ^2P^o$	0.0920		0.0670[l], 0.0109[m], 0.0051[p]
$3d^{10}8p\ ^2P^o$	0.0198		0.0714[l], 0.0084[m], 0.0043[p]
$3d^{10}9p\ ^2P^o$	0.0072		0.0548[l], 0.0040[m], 0.0016[p]
$3d^{10}5s\ ^2S$—$3d^{10}4p\ ^2P^o$	0.9172	1.327[c], 1.030[e]	1.0300[h], 1.1457[l], 0.8259[m], 0.9140[q]
$3d^{10}5p\ ^2P^o$	2.5740		2.5364[l], 2.6633[m], 2.6456[p]
$3d^{10}6p\ ^2P^o$	0.0168		0.0251[l], 0.0286[m], 0.0055[p]
$3d^{10}7p\ ^2P^o$	0.0784		0.0534[l], 0.0366[m], 0.0200[p]
$3d^{10}8p\ ^2P^o$	0.0239		0.0533[l], 0.0243[m], 0.0124[p]
$3d^{10}9p\ ^2P^o$	0.0101		0.0596[l], 0.0105[m], 0.0056[p]
$3d^{10}6s\ ^2S$—$3d^{10}4p\ ^2P^o$	0.0960	0.0698(175)[b], 0.0743[c], 0.0706[e]	0.0792[h], 0.0818[l], 0.0736[m], 0.0816[q]
$3d^{10}5p\ ^2P^o$	1.6310		1.9620[h], 1.9134[l], 1.7208[m]
$3d^{10}6p\ ^2P^o$	3.0970		3.1080[h], 2.9333[l], 3.4270[m], 3.4604[p]
$3d^{10}7p\ ^2P^o$	0.2803		0.1796[l], 0.1703[m], 0.1072[p]
$3d^{10}8p\ ^2P^o$	0.0745		0.1151[l], 0.0789[m], 0.0431[p]
$3d^{10}9p\ ^2P^o$	0.0278		0.0983[l], 0.0296[m], 0.0156[p]
$3d^9 4s^2\ ^2D$—$3d^{10}4p\ ^2P^o$	0.0501	0.0525(131)[b], 0.0544[c], 0.0521[e]	
$3d^9 4s4p(^3P^o)\ ^2F^o$	0.0245	0.0476[c], 0.0503[e], 0.0330[g]	
$3d^9 4s4p(^3P^o)\ ^2P^o$	0.0063	0.0183[e]	
$3d^9 4s4p(^3P^o)\ ^2D^o$	0.0488	0.0384[c], 0.0832[e]	
$3d^{10}4p\ ^2P^o$—$3d^{10}4d\ ^2D$	2.9400	3.039(760)[b], 4.999[c], 3.082[e]	3.57529[h], 3.0992[k], 3.3090[m], 3.3100[q]
$3d^{10}5d\ ^2D$	0.7019		0.7864[h], 0.7530[m]
$3d^{10}6d\ ^2D$	0.2843		0.2964[m]
$3d^{10}7d\ ^2D$	0.1459		0.1511[m]
$3d^{10}8d\ ^2D$	0.0856		0.0886[m]
$3d^{10}5p\ ^2P^o$—$3d^{10}4d\ ^2D$	1.0160		0.6814[m]
$3d^{10}5d\ ^2D$	2.3090		2.8212[m]
$3d^{10}6d\ ^2D$	0.6473		0.7372[m]
$3d^{10}7d\ ^2D$	0.2830		0.3145[m]
$3d^{10}8d\ ^2D$	0.1524		0.1672[m]
$3d^{10}4d\ ^2D$—$3d^{10}4f\ ^2F^o$	10.036		9.9041[m]
$3d^{10}5f\ ^2F^o$	1.4890		1.5706[m]
$3d^{10}5d\ ^2D$—$3d^{10}4f\ ^2F^o$	0.3130		0.1741[m]
$3d^{10}5f\ ^2F^o$	9.3950		8.7096[h], 8.6562[m]
$3d^{10}4f\ ^2F^o$—$3d^{10}5g\ ^2G$	18.660		18.818[h]
$3d^{10}6g\ ^2G$	2.5750		2.5913[h]
$3d^{10}7g\ ^2G$	0.8305		0.8308[h]
$3d^{10}5f\ ^2F^o$—$3d^{10}6g\ ^2G$	16.350		16.401[h]
$3d^{10}7g\ ^2G$	3.1990		3.2212[h]

Notes. Experiments: [a]Hannaford & Lowe (1983), [b]Wiese & Martin (1980), [c]Bielski (1975), [d]Siefart et al. (1974), [e]Corliss (1970), [f]Hannaford & McDonald (1978), [g]Kono & Hattori (1982). Other calculations: [h]Civiš et al. (2011b), [i]Owono Owono et al. (2005), [j]Migdałek (2002), [k]Curtis & Theodosiou (1989), [l]Carlsson (1988), [m]Lindgård et al. (1980), [n]Froese Fischer (1977; the length form), [o]Chou & Johnson (1997), [p]Zheng et al. (2000), [q]Migdałek (1978).

[a] Uncertainties in the last quoted digits are given in parentheses.

as $3d^9 4p(^{3,1}P^o)5s\ ^2P^o$ and $3d^8 4s^2(^1S)4p\ ^2P^o$. The relative photoionization cross section below the third threshold was measured by Tondello (1973) and Müller et al. (1986), but their measured results showed different variational trends with the increase of photon energy near the threshold, and hence, they are not shown in Figure 5. Above the third threshold of 0.8055 Ry, the cross section is dominantly contributed by the $3d$ subshell with a value of ∼10 Mb.

Photoionization cross sections of the Rydberg states $3d^{10}ns\ ^2S$ (n = 5–8) are shown in Figure 6. It can be seen that the ionization potential of the subshell ns decreases with the increase of the principal quantum number n and the cross section at the respective ionization threshold increases with n. For higher n, the cross section near the threshold decreases faster with the increase of photon energy, which is consistent with the basic theory of atomic structure (Cowan 1981). For photoionization of the Rydberg state with a high principal quantum number n, the cross section near the threshold tends to be hydrogenic, which reads

$$\sigma \sim n\left(\frac{\varepsilon_n}{\varepsilon_p}\right)^3, \quad (3)$$

where ε_n is the corresponding ionization potential and ε_p is the photon energy. In Figure 6, the cross section of each state

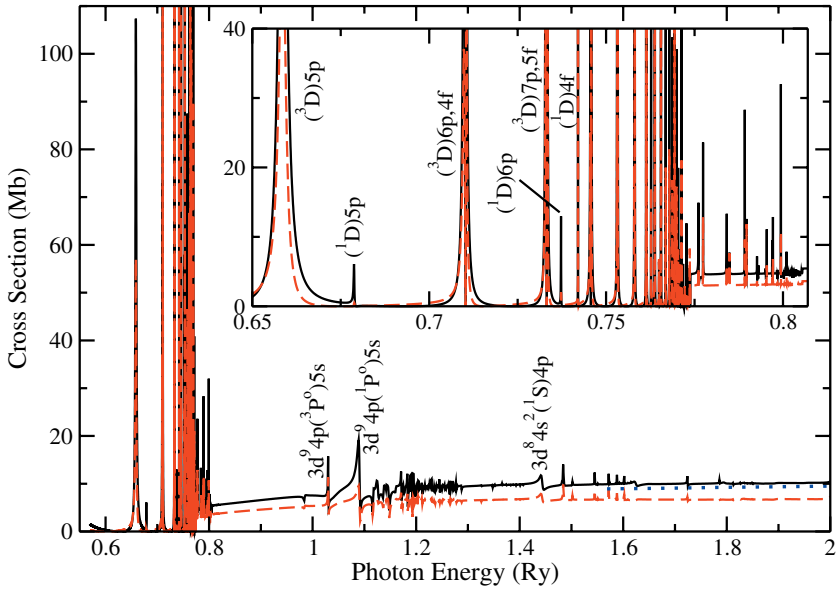

Figure 5. Photoionization cross section of the ground state $3d^{10}4s\ ^2S$. Solid and dashed lines represent the length and velocity forms, respectively, and the dotted line represents the theoretical result of Liu et al. (1994). The resonances labeled in the inset belong to $[3d^94s](^3D)np, nf$ and $[3d^94s](^1D)np, nf$.

(A color version of this figure is available in the online journal.)

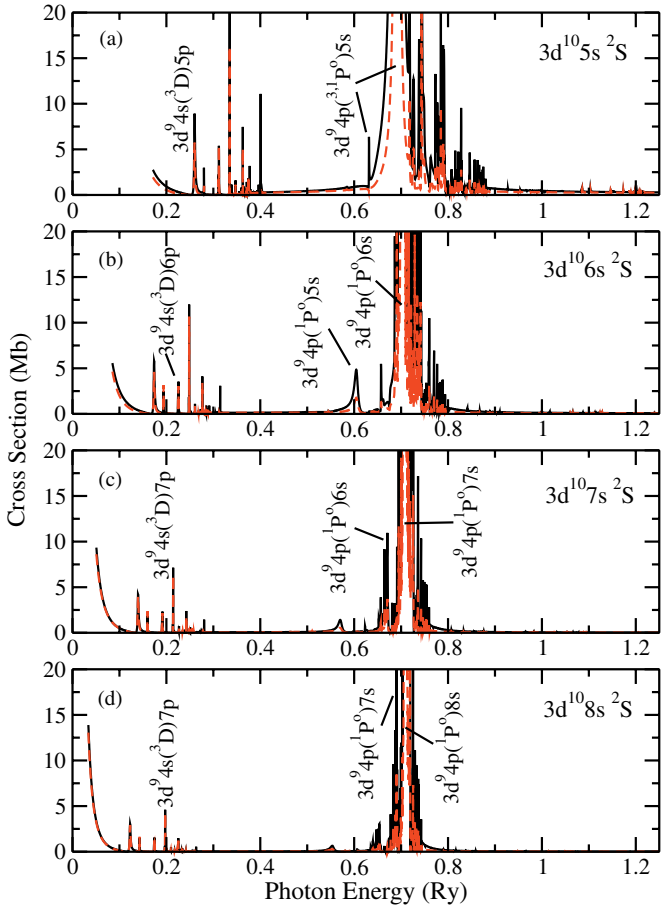

Figure 6. Photoionization cross sections of Rydberg states $3d^{10}ns\ ^2S$ ($n = 5$–8, from the top down). Solid and dashed lines represent the length and velocity forms, respectively.

(A color version of this figure is available in the online journal.)

$3d^{10}ns\ ^2S$ shows a strong resonance $3d^94p(^1P^o)ns\ ^2P^o$, which is due to the single-electron excitation from the $3d$ to the $4p$ subshell.

Inspecting Figures 5 and 6, one can see that generally good agreement is found between our length and velocity forms, especially for the cross sections of Rydberg states with higher n. For the cross section of the ground state shown in Figure 5, the two forms show a relatively larger discrepancy (about 30%). We suggest that the length form of the cross section should be more accurate.

In the following, we discuss the photoionization of the first excited state $3d^94s^2\ ^2D$, which is important for the investigation of element abundance. The partial wave $^2P^o$, $^2D^o$, and $^2F^o$ and total cross sections (in the length form) are displayed in Figure 7. For the metastable state of $3d^94s^2\ ^2D$, the ionization of $4s$ electron results in $3d^94s\ ^3D$ of Cu II, and the corresponding ionization potential is 0.6542 Ry. Because of effects of electron correlation, there are contributions to the cross sections of the partial waves $^2P^o$ and $^2F^o$ via the channels of $3d^{10}\ ^1S + kp$ and $3d^{10}\ ^1S + kf$ formed by the energetically lowest target state $3d^{10}\ ^1S$. As a result, the corresponding threshold decreases to 0.4503 Ry, which is the energy difference between $3d^94s^2\ ^2D$ of Cu I and $3d^{10}\ ^1S$ of Cu II. However, for the partial wave $^2D^o$, channels formed by $3d^{10}\ ^1S$ are impossible because of LS-coupling and parity rules, and therefore, it has contribution from 0.6542 Ry. For partial wave $^2P^o$, the cross section at 0.4503 Ry is 1.7677 Mb, which is even larger than the corresponding cross section (1.5150 Mb) of the ground state $3d^{10}4s\ ^2S$ at the threshold in Figure 5. Such a fact shows that the electron correlation is very strong for Cu I and the physical picture of a single electron is completely invalid.

It can be seen that the resonance structures in Figure 7 are rather complicated. In the region above the third threshold, $3d^94s\ ^1D$ (0.6859 Ry), the three partial waves show many strong resonances, which are attributed to the $3d$-np excitation series $3d^84s^2np$. Strong resonances make large contributions to the photoionization rate coefficients and thus will strongly influence the particle distribution in NLTE modeling

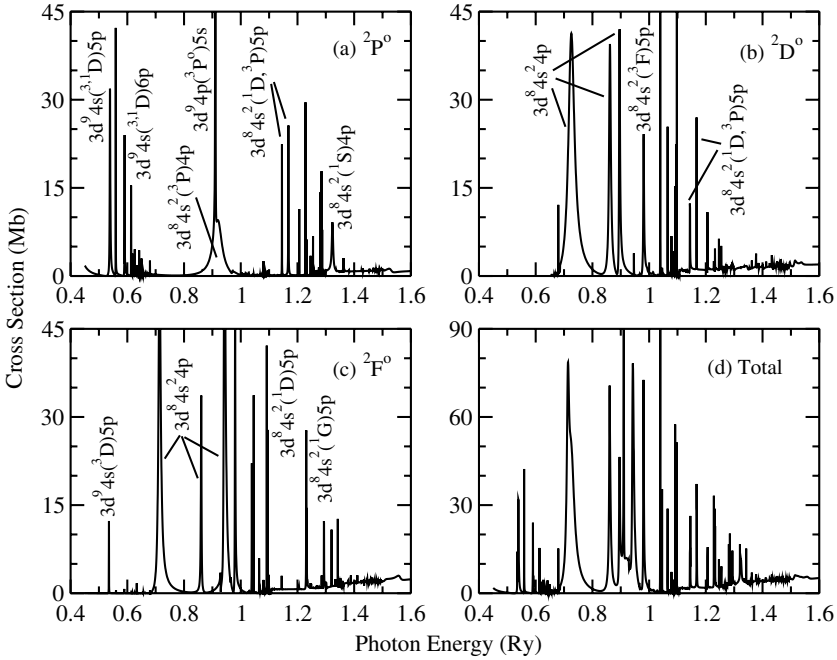

Figure 7. Partial wave and total photoionization cross sections (in the length form) of the first excited state $3d^9 4s^2\ ^2D$.

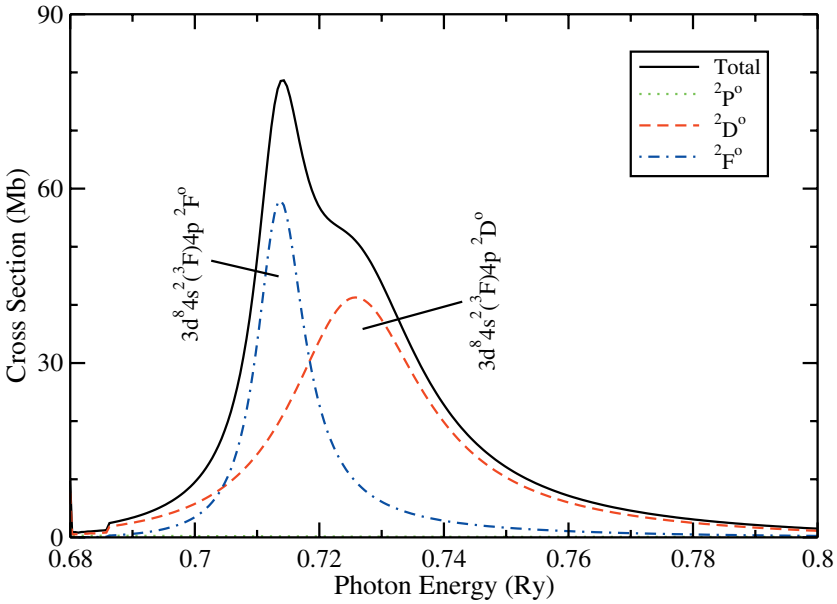

Figure 8. Same as Figure 6, but expanded to show the resonance structures of $3d^8 4s^2(^3F)4p\ ^2D^o,\ ^2F^o$ more clearly.
(A color version of this figure is available in the online journal.)

(Xiang et al. 2012). The gf value for a resonance can be obtained from the photoionization cross section by

$$gf(L_i S_i \rightarrow L_j S_j) = \frac{(2S_i+1)(2L_i+1)}{4\pi^2 \alpha a_0^2} \times \int_\Omega \sigma(\epsilon; L_i S_i \rightarrow L_j S_j) d\epsilon, \quad (4)$$

where α and a_0 are the fine-structure constant and the Bohr radius, respectively, ϵ is in rydbergs, and Ω is an energy region including the resonance in the center. L_i, S_i, L_j, and S_j are the total orbital and spin angular momenta of the initial bound terms and the final continuum states, respectively. The two strongest resonances in Figure 7 are identified as $3d^8 4s^2(^3F)4p\ ^2D^o,\ ^2F^o$ in panels (b) and (c). Their gf values are determined to be 1.7594 and 0.9972, and the autoionization widths are estimated to be 0.0253 and 0.0093 Ry, respectively. Cross sections in the vicinity of the two strongest resonances are redrawn on an expanded scale in Figure 8, where the solid line represents the total cross section, while the dotted, dashed, and dash-dotted lines represent partial waves $^2P^o$, $^2D^o$, and $^2F^o$, respectively. The contribution of $^2P^o$ is almost invisible in this region.

Turning to photoionization of the second and third excited states ($3d^{10}4p\ ^2P^o$ and $3d^9 4s 4p\ ^4P^o$) of Cu I, Figures 9 and 10 display the partial wave and total cross sections (in the length form), respectively. Both show strong resonances belonging to

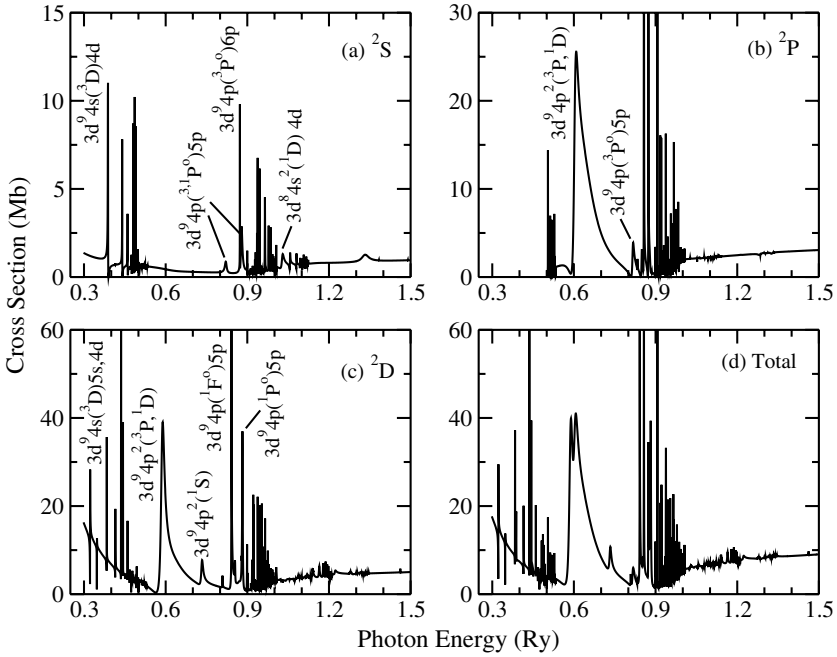

Figure 9. Partial and total photoionization cross sections of the second excited state $3d^{10}4p\ ^2P^o$.

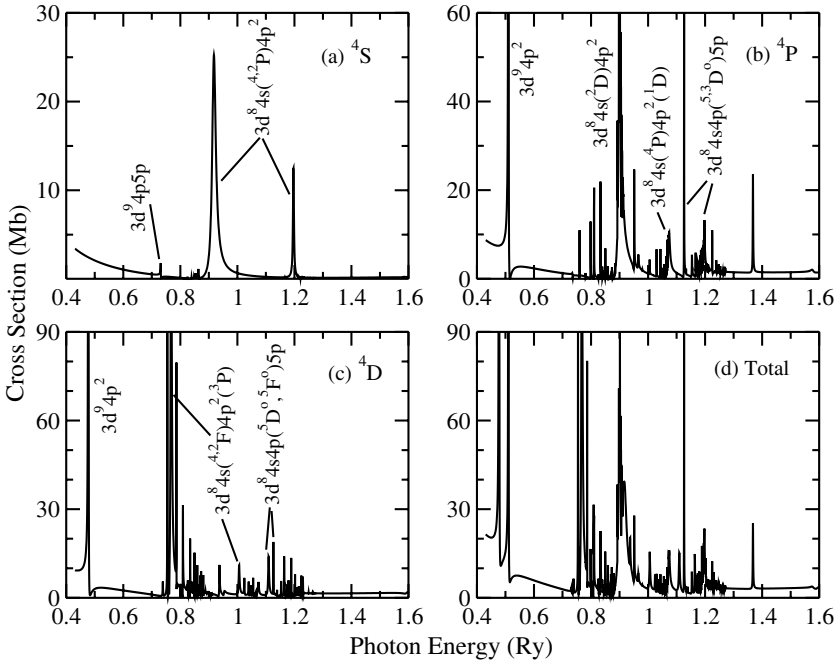

Figure 10. Partial and total photoionization cross sections of the third excited state $3d^9 4s4p\ ^4P^o$.

the configuration of $3d^9 4p^2$, but their characteristics are different. In Figures 9(b) and (c), strong and wide resonance structures appear in the partial wave ^2P and ^2D cross sections near a photon energy of ∼0.6 Ry. Each structure is contributed by two overlapping resonances, which are identified as $3d^9 4p^2(^3P)$ and $3d^9 4p^2(^1D)$ for both of the partial waves. However, for photoionization of quartet state $3d^9 4s4p\ ^4P^o$, the resonances $3d^9 4p^2\ ^4P$ and $3d^9 4p^2\ ^4D$ are much narrower, although they belong to the same configuration, $3d^9 4p^2$. Part of the reason is that the quartet resonances have fewer autoionization channels than the doublet resonances because of LS-coupling rules. The partial waves of quartet symmetries have no contributions from target states with the singlet symmetries, such as the ground state $3d^{10}\ ^1S$ of Cu II. The strongest resonances in Figure 10 are identified as $3d^8 4s(^4F)4p^2(^3P)\ ^4D$, $3d^8 4s(^2D)4p^2(^3P)\ ^4P$, and $3d^8 4s(^4P)4p^2(^3P)\ ^4S$, and all of them belong to the configuration of $3d^8 4s4p^2$.

The resonance energies of the autoionization states identified in the above figures are listed in Table 5 with respect to the ground state $3d^{10}4s\ ^2S$. The available experimental energy levels of the autoionization states in LS-coupling (Kramida et al. 2012) are also given. It can be seen that our results are in excellent agreement with the experimental data, and the largest relative difference originating from $3d^9 4s(^3D)5p\ ^2F^o$ is

Table 5
Energy Levels (in Ry) of the Autoionization States Identified from Photoionization Cross Sections of Cu I in Figures 5–10

State	This Work	NIST[a]
$3d^9 4s(^3D)5s\ ^2D$	0.5943	0.5914
$3d^9 4s(^3D)5p\ ^2F^o$	0.6549	0.6500
$3d^9 4s(^3D)4d\ ^2D$	0.6555	0.6515
$3d^9 4s(^3D)5p\ ^2P^o$	0.6586	0.6578
$3d^9 4s(^3D)4d\ ^2S$	0.6598	
$3d^9 4s(^1D)5p\ ^2P^o$	0.6788	0.6792
$3d^9 4s(^3D)6p\ ^2P^o$	0.7099	
$3d^9 4s(^3D)4f\ ^2P^o$	0.7105	
$3d^9 4s(^3D)7p\ ^2P^o$	0.7330	
$3d^9 4s(^3D)5f\ ^2P^o$	0.7334	
$3d^9 4s(^1D)6p\ ^2P^o$	0.7373	0.7397
$3d^9 4s(^1D)4f\ ^2P^o$	0.7421	
$3d^9 4p^2(^3P)\ ^4D$	0.8227	
$3d^8 4s^2(^3F)4p\ ^2F^o$	0.8334	
$3d^8 4s^2(^3F)4p\ ^2D^o$	0.8453	
$3d^9 4p^2(^3P)\ ^4P$	0.8553	
$3d^9 4p^2(^3P)\ ^2D$	0.8560	
$3d^9 4p^2(^3P)\ ^2P$	0.8751	
$3d^8 4s^2(^1D)4p\ ^2F^o$	0.9802	
$3d^8 4s^2(^1D)4p\ ^2D^o$	0.9814	
$3d^9 4p^2(^1S)\ ^2D$	1.0017	
$3d^8 4s^2(^3P)4p\ ^2D^o$	1.0150	
$3d^9 4p(^3P^o)5s\ ^2P^o$	1.0302	
$3d^8 4s^2(^3P)4p\ ^2P^o$	1.0395	
$3d^8 4s^2(^1G)4p\ ^2F^o$	1.0627	
$3d^9 4p(^3P^o)5p\ ^4S$	1.0743	
$3d^9 4p(^3P^o)5p\ ^2P$	1.0894	
$3d^9 4p(^1P^o)5s\ ^2P^o$	1.0910	
$3d^9 4p(^3P^o)5p\ ^2S$	1.0924	
$3d^8 4s^2(^3F)5p\ ^2D^o$	1.1001	
$3d^8 4s(^4F)4p^2(^3P)\ ^4D$	1.1109	
$3d^9 4p(^1F^o)5p\ ^2D$	1.1132	
$3d^9 4p(^3P^o)6p\ ^2S$	1.1442	
$3d^9 4p(^1P^o)5p\ ^2S$	1.1511	
$3d^9 4p(^1P^o)5p\ ^2D$	1.1540	
$3d^9 4p(^1P^o)6s\ ^2P^o$	1.1902	
$3d^9 4p(^1P^o)6p\ ^2S$	1.2098	
$3d^9 4p(^1P^o)7s\ ^2P^o$	1.2265	
$3d^8 4s(^2D)4p^2(^3P)\ ^4P$	1.2447	
$3d^9 4p(^1P^o)8s\ ^2P^o$	1.2452	
$3d^8 4s(^4P)4p^2\ ^4S$	1.2609	
$3d^8 4s^2(^1D)5p\ ^2D^o$	1.2635	
$3d^8 4s^2(^1D)5p\ ^2F^o$	1.2639	
$3d^8 4s^2(^1D)5p\ ^2P^o$	1.2648	
$3d^8 4s^2(^3P)5p\ ^2D^o$	1.2869	
$3d^8 4s^2(^3P)5p\ ^2P^o$	1.2875	
$3d^8 4s^2(^1D)4d\ ^2S$	1.3017	
$3d^8 4s(^2F)4p^2(^3P)\ ^4D$	1.3492	
$3d^8 4s^2(^3P)5p\ ^2F^o$	1.3507	
$3d^8 4s(^4P)4p^2(^1D)\ ^4P$	1.4158	
$3d^8 4s^2(^1S)4p\ ^2P^o$	1.4432	
$3d^8 4s4p(^5D^o)5p\ ^4D$	1.4526	
$3d^8 4s4p(^5D^o)5p\ ^4P$	1.4694	
$3d^8 4s4p(^5F^o)5p\ ^4D$	1.4694	
$3d^8 4s(^2P)4p^2\ ^4S$	1.5396	
$3d^8 4s4p(^3D^o)5p\ ^4P$	1.5409	

Note. [a] Only data of the states in LS-coupling are given.

only 0.75%. Furthermore, the present calculation shows many autoionization states beyond the threshold $3d^9 4s\ ^1D$, which are lacking in the literature both theoretically and experimentally. Photoionization cross sections of Cu I are strongly influenced by these autoionization resonances, especially those belonging to $3d^9 4p^2$, $3d^8 4s^2 4p$, and $3d^8 4s 4p^2$, which play a role in the NLTE modeling of element abundance determination.

In conclusion, energy levels, oscillator strengths, and photoionization cross sections of Cu I are calculated in the close-coupling approach within the R-matrix method for the NLTE investigation of copper abundance. We have properly treated the complex electron correlations of Cu I to ensure the accuracy of the whole data set. Our results are compared with available experimental and theoretical results in the literature. The calculated energy levels agree well with the experimental results. For the oscillator strengths of strong transitions, good agreement is obtained between our values and experimental and other theoretical results, yet a larger discrepancy was found for the weak lines. The main reason is that the oscillator strength is very sensitive to the electron correlations and different theories included different scales of CI. Photoionization cross sections of the metastable $3d^9 4s^2\ ^2D$ and other excited states are reported for the first time. Many resonances appear in the photoionization cross sections, and the positions are determined by fitting the Fano profile. The strongest ones originate from the levels belonging to the configurations of $3d^9 4p^2$, $3d^8 4s^2 4p$, and $3d^8 4s 4p^2$, which are due to the single-electron excitation from the $3d$ to the $4p$ subshell for different terms. The calculated resonance positions are in good agreement with the experimental results wherever they are available. The resonant structures are expected to have profound effects on the photoionization rate coefficients and therefore to affect the abundance determination. The complete data set, including the gf values and photoionization cross sections, is available upon request and in the online journal in machine-readable table format.

This work was supported by the National Natural Science Foundation of China under Grant Nos. 11274382, 11274383, 11204376, and 10878024.

REFERENCES

Allen, D. M., & Porto de Mello, G. F. 2011, A&A, 525, A63
Asplund, M. 2005, ARA&A, 43, 481
Baig, M. A., Hanif, M., Bhatti, S. A., & Hormes, J. 1997, JPhB, 30, 5381
Bautista, M. A. 2000, JPhB, 33, L419
Bergemann, M., Pickering, J. C., & Gehren, T. 2010, MNRAS, 401, 1334
Berrington, K. A., Eissner, B. W., & Norrington, P. H. 1995, CoPhC, 92, 290
Bielski, A. 1975, JQSRT, 15, 463
Biémont, E. 1973, BSRSL, 42, 206
Biémont, E., Fryczynski, F., Palmeri, P., Quinet, P., & Zeippen, C. J. 1996, JQSRT, 55, 215
Bisterzo, S., Gallino, R., Pignatari, M., et al. 2004, MmSAI, 75, 741
Bonifacio, P., Caffau, E., & Ludwig, H.-G. 2010, A&A, 524, A96
Brewer, M.-M., & Carney, B. W. 2006, AJ, 131, 431
Bruhn, R., Sonntag, B., & Wolff, H. W. 1979, JPhB, 12, 203
Carlsson, J. 1988, PhRvA, 38, 1702
Chou, H.-S., & Johnson, W. R. 1997, PhRvA, 56, 2424
Civiš, S., Matulková, I., Cihelka, J., et al. 2011a, JPhB, 44, 105002
Civiš, S., Matulková, I., Cihelka, J., et al. 2011b, JPhB, 44, 025002
Clementi, E., & Roetti, C. 1974, ADNDT, 14, 177
Colucci, J. E., Bernstein, R. A., Cameron, S. A., & McWilliam, A. 2012, ApJ, 746, 29
Corliss, C. H. 1970, JRNBS, 74A, 781
Cowan, R. D. 1981, The Theory of Atomic Structure and Spectra (Berkeley, CA: Univ. California Press)
Cunha, K., Smith, V. V., Bergemann, M., Suntzeff, N. B., & Lambert, D. L. 2010, ApJ, 717, 333
Cunha, K., Smith, V. V., Suntzeff, N. B., et al. 2002, AJ, 124, 379
Curtis, L. J., & Theodosiou, C. E. 1989, PhRvA, 39, 605
Froese Fischer, C. 1977, JPhB, 10, 1241

Fu, K., Jogwich, M., Knebel, M., & Wiesemann, K. 1995, ADNDT, 61, 1
Gehren, T., Shi, J. R., Zhang, H. W., Zhao, G., & Korn, A. J. 2006, A&A, 451, 1065
Hannaford, P., & Lowe, R. M. 1983, OptEn, 22, 532
Hannaford, P., & McDonald, D. C. 1978, JPhB, 11, 1177
Hibbert, A. 1975, CoPhC, 9, 141
Johnson, J. A., Ivans, I. I., & Stetson, P. B. 2006, ApJ, 640, 801
Kono, A., & Hattori, S. 1982, JQSRT, 28, 383
Kramida, A., Ralchenko, Yu., Reader, J., & NIST ASD Team 2012, NIST Atomic Spectra Database (Ver. 5.0; Gaithersburg, MD: National Institute of Standards and Technology), http://physics.nist.gov/asd
Kurucz, R., & Bell, B. 1995, CD-ROM 23, Atomic Line Data (Cambridge, MA: Smithsonian Astrophysical Observatory)
Liang, G. Y., & Badnell, N. R. 2010, A&A, 518, A64
Lindgård, A., Curtis, L. J., Martinson, I., & Nielsen, S. E. 1980, PhyS, 21, 47
Liu, J. C., Liu, Z. W., & Kelly, H. P. 1994, PhRvA, 50, 3909
Liu, Y. P., Gao, C., Zeng, J. L., & Shi, J. R. 2011, A&A, 536, A51
Mashonkina, L., Zhao, G., Gehren, T., et al. 2008, A&A, 478, 529
McWilliam, A., & Smecker-Hane, T. A. 2005, ApJL, 622, L29
Migdałek, J. 1978, JQSRT, 20, 81
Migdałek, J. 2002, PhST, 100, 47
Müller, M., Schmidt, M., & Zimmermann, P. 1986, EL, 2, 359
Owono Owono, L. C., Kwato Njock, M. G., & Owona Angue, M. L. C. 2005, PhLA, 339, 343
Romano, D., & Matteucci, F. 2007, MNRAS, 378, L59
Shi, J. R., Gehren, T., Butler, K., Mashonkina, L., & Zhao, G. 2008, A&A, 486, 303
Shi, J. R., Gehren, T., Zeng, J. L., Mashonkina, L., & Zhao, G. 2014, ApJ, 782, 80
Siefart, E., Ney, J., Bucka, H., & Bolouri, H. 1974, JPhB, 7, 1279
Simmerer, J., Sneden, C., Ivans, I. I., et al. 2003, AJ, 125, 2018
Sugar, J., & Musgrove, A. 1990, JPCRD, 19, 527
Tondello, G. 1973, JOSA, 63, 346
Verweyen, A., Donnelly, D., Hibbert, A., & Bell, K. L. 1998, PhRvA, 58, 3338
Wiese, W. L., & Martin, G. A. 1980, Wavelengths and Transition Probabilities for Atoms and Atomic Ions (Washington, DC: NSRDS-NBS), 68
Xiang, W., Gao, C., Fu, Y., Zeng, J., & Yuan, J. 2012, PhRvA, 86, 061401 (R)
Zeng, J. 2008, JPhB, 41, 125702
Zeng, J., Gao, C., & Yuan, J. 2010, PhRvE, 82, 026409
Zeng, J., Liu, P., Xiang, W., & Yuan, J. 2013a, PhRvA, 87, 033419
Zeng, J., Liu, P., Xiang, W., & Yuan, J. 2013b, JPhB, 46, 215002
Zeng, J., & Yuan, J. 2006, PhRvE, 74, 025401 (R)
Zeng, J., & Yuan, J. 2007, PhRvE, 76, 026401
Zheng, N., Wang, T., & Yang, R. 2000, JChPh, 113, 6169